



Determination of absolute material nonlinearity with air-coupled ultrasonic receivers



David Torello^{a,*}, Nicholas Selby^a, Jin-Yeon Kim^b, Jianmin Qu^c, Laurence J. Jacobs^{a,b}

^a GW Woodruff School of Mechanical Engineering, Georgia Institute of Technology, Atlanta, GA 30332, United States

^b School of Civil and Environmental Engineering, Georgia Institute of Technology, Atlanta, GA 30332, United States

^c Department of Mechanical Engineering, Tufts University, Medford, MA 02155, United States

ARTICLE INFO

Article history:

Received 14 November 2016

Received in revised form 24 May 2017

Accepted 1 June 2017

Available online 3 June 2017

Keywords:

Nonlinear acoustics

Nondestructive evaluation

Air-coupled ultrasonics

ABSTRACT

Quantitative evaluation of the microstructural state of a specimen can be deduced from knowledge of the sample's absolute acoustic nonlinearity parameter, β , making the measurement of β a powerful tool in the NDE toolbox. However, the various methods used in the past to measure β each suffer from significant limitations. Piezoelectric contact transducers are sensitive to nonlinear signals, cheap, and simple to use, but they are hindered by the variability of the interfacial contact between transducer and specimen surface. Laser interferometry provides non-contact detection, but requires carefully prepared specimens or complicated optics to maximize sensitivity to the higher harmonic components of a received waveform. Additionally, laser interferometry is expensive and relatively difficult to use in the field. Air-coupled piezoelectric transducers offer the strengths of both of these technologies and the weaknesses of neither, but are notoriously difficult to calibrate for use in nonlinear measurements. This work proposes a hybrid modeling and experimental approach to air-coupled transducer calibration and the use of this calibration in a model-based optimization to determine the absolute β parameter of the material under investigation. This approach is applied to aluminum and fused silica, which are both well-documented materials and provide a strong reference for comparison of experimental and modeling results.

© 2017 Elsevier B.V. All rights reserved.

1. Introduction

Nonlinear ultrasonic (NLU) techniques have been successfully used to characterize material defects and microstructural evolution through various aging and deformation mechanisms such as fatigue [1–4], cold work [5], thermal aging [6,7], creep [8], and radiation exposure [9] dating as far back as the 1960s [10–17]. These measurements all seek to capitalize on the change in the nonlinear stress-strain relationship that occurs as a material undergoes microstructural changes by measuring the distortion of ultrasonic waves as they propagate through the sample. Second harmonic generation (SHG) is a technique in the field of NLU where a monotonic ultrasonic input generates additional waves at harmonics of the input frequency as it propagates through the specimen. The second harmonic wave amplitude (A_2) is compared to the square of the fundamental amplitude (A_1^2), and the ratio of these two amplitudes is proportional to the acoustic nonlinearity parameter, β . This β value can be correlated to the change in mate-

rial microstructure due to external effects, and when this parameter is tracked over time or damage evolution, a useful picture of the material life (past and remaining) can be constructed that may inform engineering decisions regarding a variety of materials and situations.

In order to determine the state of a material sample, tests are often performed relative to a base, unaltered state and the SHG measurements are tracked as the material state evolves [9,18–20]. This type of measurement is referred to as a relative nonlinearity measurement and is typically performed with uncalibrated acoustic transducers that measure the relative acoustic nonlinearity parameter β^* . This approach is used simply because the absolute signal amplitudes do not matter when the change in those amplitudes is the desired measurement result. While useful when an unaltered sample of the material is present, there are vastly more situations in which this condition cannot be met such as in existing transportation or public utilities infrastructures. In these cases, approaching a sample with no prior knowledge of the material requires the measurement of the absolute nonlinearity parameter β , which can be used to predict material state through modeling and, by extension, remaining material life.

* Corresponding author.

E-mail address: david.torello@gmail.com (D. Torello).

Many receiver technologies exist that can easily provide relative SHG measurements effectively and cheaply, most notably contact piezoelectric transducers [2,9,18,21]. These piezoelectric devices exhibit high sensitivity and desirable electronic and mechanical properties for use in NLU experiments, but because they are resonant devices they exhibit frequency dependent electroacoustic transfer functions that must be known to accurately interpret their responses to ultrasonic inputs [22,23]. Contact piezoelectric transducers can be calibrated to provide absolute signal measurements [24–26], but there are some significant limitations associated with these calibrations. First, the calibration of contact transducers is dependent on the interface conditions between the transducer and the sample, typically through a fluid couplant layer which is extremely difficult to control. Because the transducer and fluid couplant layer are calibrated together, a new calibration must be performed every time the couplant layer changes, which occurs with every new contact measurement. Additionally, if the coupling of the transducer and the sample is poor, the electroacoustic transfer function obtained from experiment may be meaningless because of poor signal quality, harmonic generations from contact, etc [27,28]. While absolute measurements with contact piezoelectric transducers are certainly possible [2], a much more effective and robust approach is the use of non-contact receivers to measure the fundamental and second harmonic wave amplitudes.

Non-contact detection has been used for performing absolute SHG measurements with many receiving technologies, including capacitive electrostatic transducers [7,17,29–31], EMATs [32,33], and laser interferometers [21,30,34,35]. These techniques all have their advantages and disadvantages, but when it comes to measuring across a variety of samples under in-situ conditions with the greatest ease, laser interferometry is the most effective of these technologies. However, laser interferometers are expensive, bulky, and benefit from highly polished samples or reflective surfaces for effective use in detecting higher harmonic waves [34,36] which ultimately detracts from their usefulness in field applications.

A very attractive alternative to laser interferometry is the use of air-coupled piezoelectric transducers, which exhibit the high sensitivity and low relative cost of contact piezoelectric transducers, and are well adapted for use in in-situ applications where laser interferometry would struggle. Electromechanical calibration of the transducer has proven elusive for use in SHG measurements up to this point, but because the couplant in this case is a repeatably controllable air gap, a single calibration of the transducer remains viable for all subsequent measurements. This work provides the necessary theoretical and experimental frameworks to adapt air-coupled transducers for use in measuring absolute β , equipping the NDE community with a much needed tool for absolute NLU inspection of previously difficult to measure specimens in a broader variety of experimental conditions. A combination of modeling and experimental results are used to calibrate the receivers, and the calibrated transducers are combined with a nonlinear optimization routine to measure the absolute β of aluminum 2024 and fused silica samples. These results are finally compared to similar results from existing literature, providing a benchmark for the effectiveness of the proposed techniques.

This paper is laid out in the following structure. First, a modeling framework for predicting the fundamental and second harmonic wave fields from generating to receiving transducer is proposed, including a discussion of general concepts for modeling nonlinear wave fields through stacks of multiple materials. Next, a discussion of nonlinear optimization provides a use for the modeling equations in determining the absolute acoustic nonlinearity. Next, a combination of modeling and experimental results are used to calibrate the receivers, and the calibrated transducers are combined with the nonlinear optimization routine to measure the absolute β of aluminum 2024 and fused silica samples. These

results are finally compared to similar benchmark results from literature as validation of the proposed techniques.

2. Theoretical background

A schematic of longitudinal wave SHG measurements is shown in Fig. 1. The basic principle of the SHG technique is measuring the second harmonic and fundamental wave amplitudes and using them to calculate the material nonlinearity β . In the case of the contact transducer setup of Fig. 1(a), simply calibrating the transducer so as to convert a received displacement or strain to an electric current or voltage is sufficient to capture the absolute surface displacements from the transducer electrical outputs. However, the air-coupled transducer of Fig. 1(b) is not performing a direct surface measurement, but rather an indirect measurement of the leaked pressure waves from the surface vibrations of the sample. In order to extract the surface information from the measured electrical output of the air-coupled receiver, additional steps must be taken to relate the conditions on the surface of the sample to the conditions on the surface of the receiver face. In this work, a model based approach is used to link these quantities which is comprised of three distinct parts: (1) A propagation model to account for the leakage of acoustic waves from the sample surface, (2) an optimization routine based on this model to solve for sample surface displacements from measured voltage data from the transducer, and (3) a calibration of the transducer to correctly map output voltage to the acoustic conditions on the receiver surface.

2.1. Longitudinal propagation modeling

2.1.1. Second harmonic generation theory

An in-depth summary of second harmonic generation (SHG) techniques for NLU [37] describes the mechanisms behind the

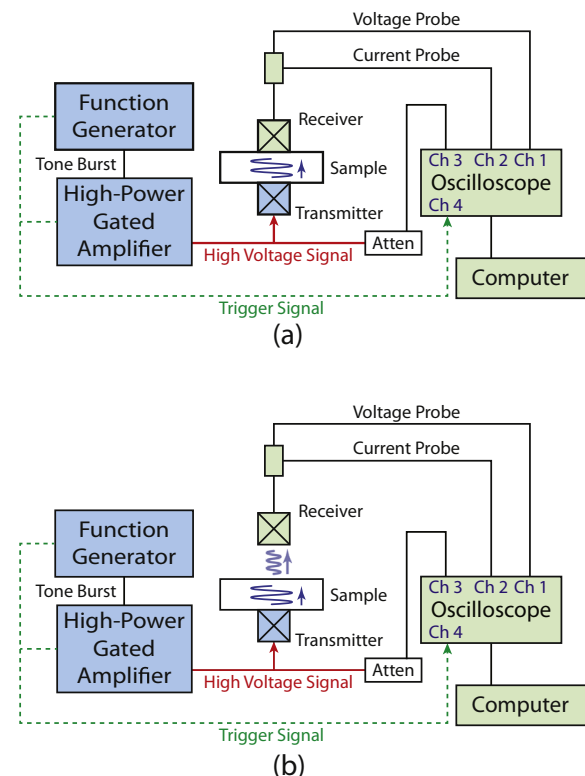


Fig. 1. Experimental setup schematic of longitudinal wave SHG measurements for the determination of material nonlinearity. (a) Piezoelectric contact transducer used as the ultrasonic receiver. (b) Air-coupled piezoelectric transducer used as the ultrasonic receiver.

development of higher harmonic signals as a monochromatic fundamental signal propagates through a sample. For SHG techniques, and most nonlinear ultrasonic tests in general, the ultimate goal is to measure the nonlinearity parameter β , which can be found by comparing the magnitudes of the fundamental and second harmonic wave components detected by a receiver after the ultrasonic signal has propagated a distance x via the following relationship:

$$\frac{(A_2)^{\text{el}}}{(A_1^2)^{\text{el}}} = \beta^* x \quad (1)$$

In Eq. (1), the term β^* denotes the relative acoustic nonlinearity parameter that is obtained from uncalibrated measurements, usually the direct voltage or current outputs of the receiver during the experiment. Practically, this expression is convenient because it affords many possible ways of measuring the nonlinearity parameter, and measures of uncalibrated values of $(A_1^2)^{\text{el}}$ and $(A_2)^{\text{el}}$ can quickly provide the relative nonlinearity parameter β^* . In longitudinal wave measurements, the variable x is usually fixed, which means that the determination of β^* is done by varying the input fundamental amplitude and plotting A_2 by A_1^2 , taking the linear slope as the value of the nonlinearity parameter.

If the measured amplitudes are absolute amplitudes resulting from proper system calibration, the expression for the absolute nonlinearity parameter looks as follows:

$$\frac{A_2}{A_1^2} = \frac{\beta k^2 x}{8} \quad (2)$$

The goal of this work is to use air-coupled piezoelectric ultrasonic transducers, which have historically only been used to calculate β^* as in Eq. (1), to calculate the absolute material nonlinearity β as in Eq. (2). This will require more careful characterization of the ultrasonic field from transmitter to receiver as well as a careful calibration of the receiver itself.

2.1.2. Attenuation and diffraction corrections

It is important to note that the expression for the nonlinearity parameter given in Eq. (2) ignores the effects of diffraction and attenuation, which over large propagation distances or in the near field will have significant effects on measurement results. The Khokhlov-Zabolotskaya-Kuznetsov (KZK) equation was developed to account for these effects and takes the form [38]:

$$\frac{\partial^2 p}{\partial z \partial \tau} = \frac{c}{2} \nabla_{\perp}^2 p + \frac{\delta}{2c^3} \frac{\partial^3 p}{\partial \tau^3} + \frac{\beta}{2\rho c^3} \frac{\partial^2 p^2}{\partial \tau^2} \quad (3)$$

where p is the acoustic pressure, τ is the retarded time $\tau = t - (z/c)$, δ is the sound diffusivity dependent on viscosity, thermal conductivity, and specific heat terms, ∇_{\perp}^2 is the transverse Laplacian in x , y coordinates, and z is the beam propagation direction. The first term on the right-hand side of Eq. (3) models the diffraction of the propagating wave, the second term models the dissipation, and the third term models the generation of harmonic wave components due to material nonlinearity. Central to the formulation of Eq. (3) is the use of paraxial approximation, which necessarily breaks down in regions close to the source. However, the validity of this approximation has been tested in transducer beam field modeling and for regions half of a source diameter from the source itself, the approximation is acceptably close to the actual solution [39].

Assuming a quasilinear solution to the KZK equation, the following equations of motion for the fundamental and second harmonic wave fields can be found:

$$\frac{\partial p_1}{\partial z} + \frac{i}{2k} \nabla_{\perp}^2 p_1 + \alpha_1 p_1 = 0 \quad (4)$$

$$\frac{\partial p_2}{\partial z} + \frac{i}{2k} \nabla_{\perp}^2 p_2 + \alpha_2 p_2 = \frac{\beta k}{2\rho c^2} p_1^2 \quad (5)$$

where p_1 is the fundamental frequency component amplitude, p_2 is the second harmonic component amplitude, and α_n is the attenuation of an acoustic wave propagating linearly through a material at the n^{th} harmonic, with $n = 1$ corresponding to the fundamental wave form and $n = 2$ corresponding to the second harmonic waveform. This distinction is important because the actual attenuation of the second harmonic waveform is more complicated than the attenuation of a linearly propagating wave at a frequency 2ω which will be shown in the next section.

2.1.3. Multiple Gaussian beam modeling

Wen and Breazeale [40] took the idea of discretizing sources as a linear combination of the Gaussian beams from optics and applied it to ultrasonic piston-like transducers by finding Gaussian coefficients A_n and B_n such that, at the source, the pressure can be modeled as

$$p_1(r, 0) = \sum_{n=1}^N p_0 A_n \exp(-B_n r^2 / a^2) \quad (6)$$

where a is the source radius and r is the radial distance from the source center. A set of 15 coefficients was determined to accurately model a piston transducer and the resulting field from as little as a distance a from the source with a high degree of accuracy [39]. This modeling scheme has major advantages over the exact solution obtained from a method such as the Rayleigh-Sommerfeld Integral (RSI) approach. The first major advantage is that the wave field for propagation through multiple materials can be found very easily in one global ABCD matrix approach for the linear portion of the wave field [41]. Another major advantage of this approach is that the full-field solution for each individual Gaussian term is analytical, which means that the full field from the piston transducer is solved with one integration of a modest number of terms [42,43]. The RSI integral requires fine discretization of the source and receiver, which is essentially a quadruple integral over a domain that depends on the wavelength of the propagating wave. This gain in computational efficiency is very important for the later aspects of this work and is the primary choice for using this modeling framework for future steps.

The Multiple Gaussian Beam (MGB) modeling framework has been adapted for nonlinear wave fields created by SHG, solving both Eqs. (4) and (5) using the source function of Eq. (6) and a Green's function approach [43]. The pertinent results from this published work are the following solutions for the fundamental and second harmonic wave fields:

$$p_1(z) = [p_0] [e^{-\alpha_1 z}] \left[\sum_{n=1}^N \frac{A_n}{1 - iB_n z / D_R} \exp \left(\frac{B_n (r/a)^2}{1 - iB_n z / D_R} \right) \right] \quad (7)$$

$$p_2(z) = \left[\frac{\beta k z}{2\rho c^2} p_0^2 \right] \left[\frac{\exp(-2\alpha_1 z) - \exp(-\alpha_2 z)}{(\alpha_2 - 2\alpha_1)z} \right] \times \frac{1}{z} \int_0^z \sum_{m=1}^N \sum_{n=1}^N \frac{-2A_m A_n B_b}{(2z + B_a)z' + B_a z - 2B_b} \times \exp \left\{ -2ikr^2 \left(\frac{(z'^2 + B_a z' - B_b)/(z - z')}{(2z + B_a)z' + B_a z - 2B_b} \right) \right\} dz' \quad (8)$$

where $B_a = i(B_m + B_n)/D_R$, $B_b = B_m B_n / D_R^2$, and $D_R = ka^2/2$ is the Rayleigh distance denoting transition from the near field to the far field of the acoustic source. Eqs. (7) and (8) provide a complete accounting of the wave fields for the fundamental and second harmonic waves as they propagate through a single material from a finite radius piston-like source. However, as is shown in Fig. 1(b), a second material, in this case air, must be accounted for in the propagation path between the transmitting source and the receiving air-coupled transducer. In this work, we have extended the nonlinear

formulation of this MGB model to propagate through multiple layers, shown in Fig. 2(a) and (c). An optimization algorithm is used to re-derive the source function for the linear and nonlinear fields at the interface between material 1 and material 2, depicted in Fig. 2(b) and (d) respectively. These new coefficients are then used as the inputs to Eqs. (7) and (8) above, which provides the total pressure field model for propagation in air.

One of the consequences of this formulation is that for both the fundamental and second harmonic waves, a linearly and nonlinearly propagating wave component is produced in the next material as shown in Fig. 3; of particular interest is how the second harmonic wave propagates through the second material in this schematic. In previous works [20], we have shown that for sources where there is an initial nonlinear component, the initial second harmonic component of the signal propagates as if it were a fundamental frequency wave at a frequency of 2ω . The interface between materials 1 and 2 in this problem can be thought of as a new “effective source” with coefficients $A_{\text{int},2,N}$ and $B_{\text{int},2,N}$ as shown in Fig. 2(a) and (c), where the subscript “int” represents their location at the interface, the numbers 1 and 2 represent the fundamental and second harmonic respectively, and N is the number of the coefficient in the set of newly derived coefficients. Again, an N of 15 shows excellent agreement with the wave fields at the interface as can be seen in Fig. 2(b) and (d). This is a very flexible approach to solving this problem because it works irrespective of the source profile (piston, Gaussian, etc.).

Additionally, one of the consequences of Eq. (8) is that the number of terms resulting from the summations squares each time the calculation is performed because of the double summation in the diffraction correction. For example, a discrete source of 15 terms necessitates a second harmonic diffraction correction of 225 terms.

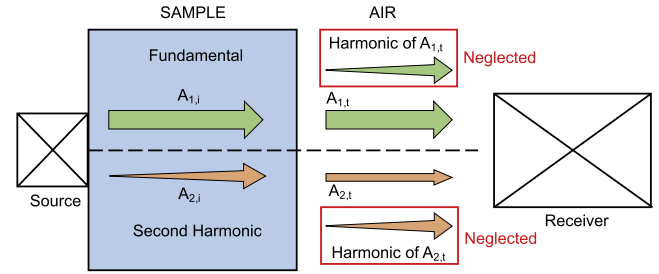


Fig. 3. Schematic of the interface between solid and air diagramming the relevant incident and transmitted waves. Note that A_2 propagates as a second harmonic wave with generation in the solid, but after transmission into the air, acts as a fundamental wave. Once the waves reach the receiver, they are integrated across the face of the transducer to obtain the force on the transducer face.

When the fundamental and second harmonic wave-fields transmit across a material boundary, the number of total coefficients would square again because of the generation of higher harmonics from both the fundamental and second harmonic waves in the first material. A large stack of materials would quickly overwhelm most computational resources. By collapsing the wave field components, particularly of the second harmonic, to a new set of 15 coefficients down from 225, this problem is neatly side-stepped.

To select which field components dominate the fundamental and second harmonic fields of $p_{1,\text{air}}$ and $p_{2,\text{air}}$, we acknowledge that the transmission coefficient T at the interface between a metallic or silica specimen and air is very small. For an aluminum 2024/air interface, T is equal to $0.985\text{e-}4$, and for a fused silica/air interface, T is equal to $1.28\text{e-}4$. This can be interpreted as a representation of

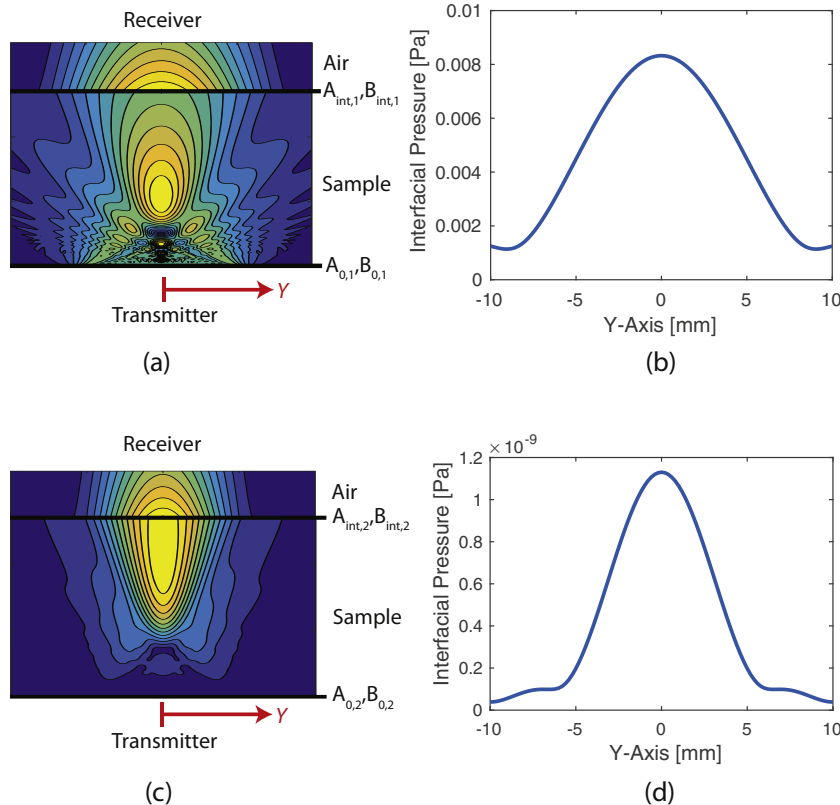


Fig. 2. Schematic of the pressure fields for fundamental and second harmonic waves propagating through a sample. Parts (a) and (c) show the wave fields for propagation starting at the transmitter at the bottom, traveling to the air/sample interface ($A_{\text{int},n}, B_{\text{int},n}$), transmitting into air, and impinging on the receiver surface at the top. Parts (b) and (c) show the pressure magnitude of the waves in air just after transmission across the interface calculated by Eq. (6) using the coefficients ($A_{\text{int},n}, B_{\text{int},n}$). Note that A_2 propagates as a second harmonic wave (Eq. (8)) with generation in the sample, but after transmission into the air, propagates as a fundamental wave (Eq. (7)).

the insertion loss of the air gap between the receiver and the sample surface as it directly relates the pressure of the propagating waves in the sample material to the pressure of the wave propagating through the air. Because of these high insertion losses caused by the low values of T , the second harmonic generated by the transmitted fundamental wave component and especially the higher harmonics generated by the transmitted second harmonic wave are neglected due to their very small magnitude. This is shown pictorially in Fig. 3 where the red-boxed components are neglected because of their low magnitude relative to the other transmitted wave components. This leaves the transmitted fundamental wave accounting for $p_{1,\text{air}}$ and the linearly propagating transmitted second harmonic wave accounting for $p_{2,\text{air}}$, summarized in the equations below:

$$p_{1,\text{air}} = T \left[p_{1,\text{metal}} \Big|_{z=L} \right] M_1(\alpha_{1,\text{air}}, z_{\text{air}}) D_1(a, f, z_{\text{air}}) \quad (9)$$

$$p_{2,\text{air}} = T \left[p_{2,\text{metal}} \Big|_{z=L} \right] M_1(\alpha_{2,\text{air}}, z_{\text{air}}) D_1(a, 2f, z_{\text{air}}) \quad (10)$$

where L is the length of propagation through the sample.

Another important consideration is the effect of the boundary between metallic specimen and air on the phase of the transmitted pressure waves. For normal incidence of a plane wave on an interface between a material with a high acoustic impedance (metal) to a material with much lower acoustic impedance (air), a reflected wave will incur a 180 degree phase shift because the reflection coefficient will have a negative value approaching $R = -1$. However, the transmission coefficient will have a positive sign regardless of its magnitude, and thus transmitted waves across the boundary will transmit in-phase and will not need a sign adjustment [44]. While the incidence of the propagating waves near the edges of the propagating beam may not exhibit plane wave behavior precisely, the diffraction correction takes into account the spatial distortions that these edge waves experience and allows us to assume normal incidence for the entire wave front.

An example of the full modeling picture is given in Fig. 4 which shows a cross-section of an aluminum sample of 27 mm thickness and an adjoining air-column of 5 mm thickness through which the acoustic pressure wavefield propagates for both the fundamental (a,c) and second harmonic (c,d) frequencies. The second harmonic generation effect is clearly demonstrated in Fig. 4(c), which is the representation of Eq. (8). Additionally, the linear propagation of the transmitted pressure waves as denoted by Eqs. (9) and (10) are shown clearly in Fig. 4(b) and (d), with the signal attenuating and diffracting leading a monotonic amplitude decrease with propagation distance.

When the air-coupled transducer of Fig. 1(b) receives the pressure wave propagating through the air column as in Fig. 4(b) and (d), it is responding to the total received force from the pressure field distribution across the surface of the transducer, which causes a strain through the piezoelectric element and thus a voltage from the piezoelectric effect. Therefore, the final piece of the modeling is to calculate the force on the transducer face, which is accomplished by simply integrating the pressure field across the surface of the transducer:

$$F_n(x', y') = 2 \int_A p_n(x, y) dA \quad (11)$$

where A is the surface area of the receiving transducer element. The coordinate pair (x', y') is used to denote the center of the air-coupled transducer, which when scanned in the $x-y$ plane averages the pressure field across the transducer surface area centered at that location. The multiplication by 2 accounts for the fact that the transducer face is essentially a rigid boundary due to the high impedance mismatch between the transducer and the surrounding air.

A plot demonstrating the difference in the received force from the air-coupled transducer versus the actual pressure distribution across the transducer face is given in Fig. 5. Notably, the received force as a function of position has a much broader/flatter shape than the pressure distribution. This is due to the finite size of the receiver which essentially creates a moving average weighted by the modal response of the transducer element as contrasted to a point-like receiver such as a laser interferometer. For the frequencies of interest, the modal response of the transducer is assumed to be piston-like because the frequencies of interest are below or near the transducer fundamental resonance. This step completes the forward model from source transducer to receiving transducer.

2.2. Inverse problem and optimization algorithm

Ultimately, we need to take measured voltages from the air-coupled transducer and use these voltages to infer the surface vibration amplitudes on the sample. This type of measurement fits neatly into an inverse problem formulation that can be solved numerically using nonlinear least-squares optimization [20,30]. The cost function for this optimization is the calculated force on the surface of the air-coupled receiver due to the radiation of the pressure waves from the surface of the metallic sample derived in the previous section. The process of nonlinear least squares optimization solves the cost function given input values of the problem variables $F_n(p_0, \alpha_1, \alpha_2, a, f, \beta)$ and iterates those values in a methodical manner until the calculated force on the air-coupled transducer surface matches experimentally determined values. This is stated mathematically in Eq. (12).

$$\begin{aligned} \min_{\{p_{0,n}, \alpha_n, \beta\} \in \mathfrak{R}} \|F_n(\{p_{0,n}, \alpha_n, \beta\}, x, y) - F_n^{\text{MEAS}}\|_2^2 \\ = \min_{\{p_{0,n}, \alpha_n, \beta\} \in \mathfrak{R}} \sum_i [F_n(\{p_{0,n}, \alpha_n, \beta\}, x_i, y_i) - F_{n,i}^{\text{MEAS}}]^2 \end{aligned} \quad (12)$$

where F_n represents the force calculated through integration of Eqs. (9) and (10) over the receiver surface for the n^{th} harmonic and F_n^{MEAS} represents the measured forces at these harmonics.

An important facet of this optimization is that instead of using data from one measurement along the acoustic axis of the generated and receiving transducers as in a typical contact measurement, the entire measurement field consisting of discrete scan points is used. This field measurement based reconstruction is advantageous over a single measurement reconstruction because the redundancy provided by multiple measurements helps to avoid convergence on local minima and provides a more stable result representative of the correct values. When using a single measurement point, there is a possibility of multiple solutions to the set of minimization variables that may provide similar values of the cost function, which is avoided in the field measurement based reconstruction approach.

The optimization process is broken up into two steps, solving Eq. (12) for $n = 1$ (the fundamental) first, which only relies on the variables $\{p_0, \alpha_1\}$, and then solving using the curve-fit solutions for those variables as inputs for solving the optimization equation for $n = 2$ (the second harmonic). The second harmonic depends on the variables $\{p_0, \alpha_1, \alpha_2, \beta\}$, only two of which are still unknown. By completing the optimization in two steps, we reduce the number of optimization variables for each part of the problem, increasing the likelihood of convergence. By choosing appropriate guess values based on knowledge of the materials involved, the convergence speed of the nonlinear least-squares algorithm is greatly increased, and convergence on local minima can be avoided.

After the optimization of the second harmonic information is completed, the output of the algorithm includes the sought-after parameter β . If the experimental force values F_n^{MEAS} are properly

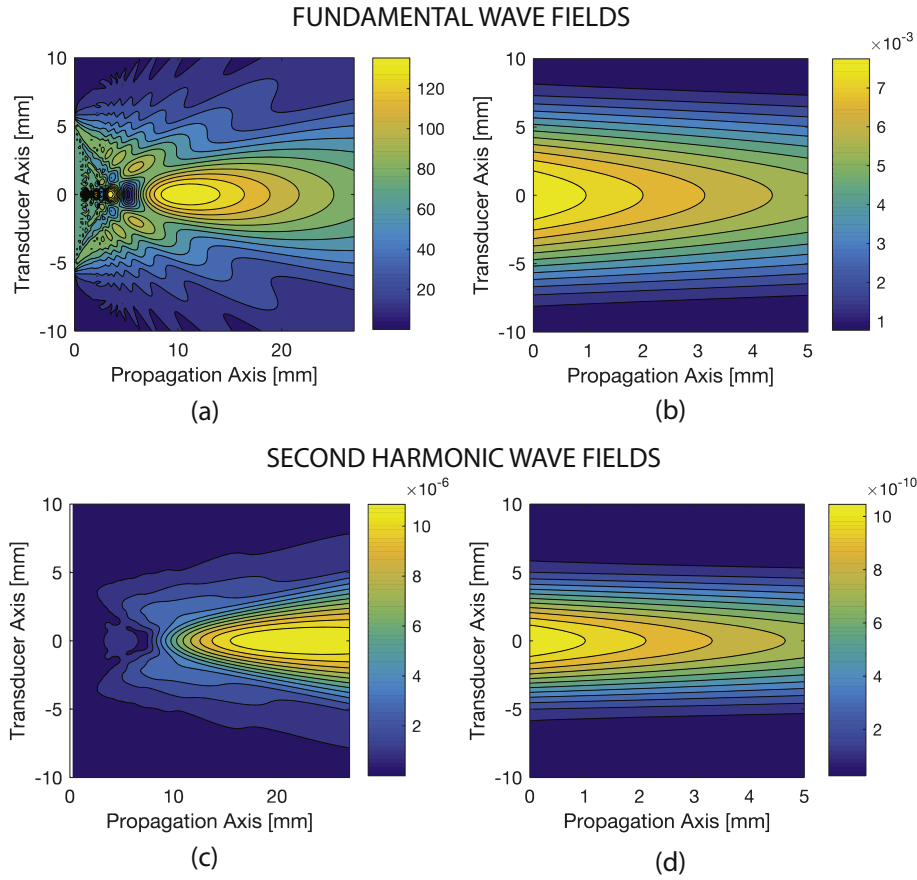


Fig. 4. Contour map representation of the calculated wave fields in aluminum and air for the fundamental and second harmonic fields. The fundamental wave field for aluminum is shown in (a) and the fundamental wave field of the transmitted wave through air is shown in (b). Similarly, the second harmonic wave field in aluminum is shown in (c) and the second harmonic wave field of the transmitted wave through air is shown in (d). The contour lines are meant to highlight the diffraction and attenuation effects of the field components.

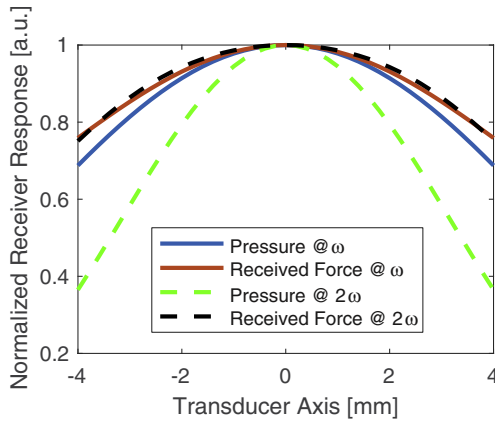


Fig. 5. Plot demonstrating the differences in the apparent shapes of the pressure waves in the air column and the received force value when the center of the transducer is located at the same position. Both the fundamental (solid) and second harmonic (dashed) quantities are displayed.

calibrated values based on the transfer function of the receiving transducer, then the value of β that results from the algorithm of Eq. (12) will be the absolute β of the material. Careful calibration of the air-coupled transducer is therefore very important, and is discussed in the next section.

2.3. Transducer calibration

Piezoelectric transducer calibration can be performed in several ways, but the easiest way to calibrate a transducer based on the number of measurements required is the self-reciprocity calibration, which uses a pulse-echo configuration to derive the relationship between the displacement of the acoustic wave at the transducer face and the transducer's electrical output. For contact transducers, this is a practical and robust way to determine the transducer response because the transducers can transmit relatively large amplitude waves via large electrical input signals, allowing for high signal to noise ratios (SNR) on the received echos. This is crucial for obtaining clean calibration curves using self-reciprocity techniques. Air-coupled transducers cannot take the same level of input power as a contact transducer per the manufacturer's operation recommendations, suffers from high insertion loss in air, and the pulse echo setup broadcasts acoustic waves through air instead of a less lossy medium, all of which results in very small amplitude received echos and very low SNR. Calibrations resulting from self-reciprocity techniques are thus much more difficult to make with air-coupled transducers and generally produce untrustworthy results.

To avoid this problem, we have developed a model-based calibration technique shown schematically in Fig. 6 in which a known aluminum 2024 calibration specimen that is fully characterized at the frequencies of interest is used as a source in an MGB model to predict the pressure wave amplitude at the face of the transducer.

These received waves are integrated across the receiver surface to provide the force on the transducer as in Eq. (11), which is then related to the electrical output of the transducer from experimental measurements. This provides a force to voltage calibration which can be used to convert the relative amplitudes of the fundamental and second harmonic waves to absolute amplitudes based on the received forces as discussed in Section 2.2. A sample calibration curve obtained from this process is shown in Fig. 7. This is the last piece of the puzzle required to extract absolute β measurements from experimental air-coupled transducer data.

3. Experimental setup and procedure

3.1. Experimental Setup

The experimental setup is shown schematically in Fig. 1(b). A toneburst signal of 12 cycles is generated by an Agilent 33250A signal generator at 2.1 MHz, which is fed to a Ritec SNAP 5000 high power gated amplifier to amplify the input signal to 1000 Vpp with a pulse repetition rate of 20 ms. The signal is passed to the generating transducer, which is held in contact with the sample by a toggle clamp and positioned by the test apparatus. The transducer generates the acoustic signal which propagates through the sample, transmits into the air, and arrives at the face of the air-coupled receiver. The receiver is an Ultran NCT4-D13 piezoelectric transducer with a center frequency of 3.9 MHz and diameter of 12.5 mm.

The receiver is attached to a five axis scanning stage and held above the sample with a standoff height of 5 mm. For laser interferometry scans, the air-coupled receiver is replaced with a Polytec LDV which is used for verification measurements of the sample surface displacements. The Polytec model used in this work is the OFV-534 compact optical head in conjunction with an OFV-5000 controller equipped with the DD-300 displacement decoder, which has a flat measurement bandwidth up to 20 MHz.

Two different samples are used in these experiments: a 27 mm thick plate of aluminum 2024, and a 19 mm thick specimen of fused silica. Additionally, a different generating transducer was used for each specimen. The aluminum sample is excited by a Panametrics V106 commercial contact transducer with a nominal center frequency of 2.25 MHz and a half inch diameter. The fused silica sample is excited by a lithium niobate (LiNbO_3) disc with a center frequency of 2 MHz and a half inch diameter.

While the air-coupled transducer is fairly insensitive to minor surface blemishes on the specimens, the laser LDV is not and requires a mirror-like reflectivity in order to have the SNR required to make second harmonic measurements. In order to make the alu-

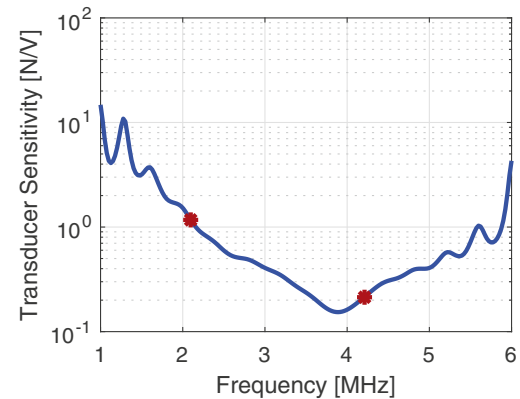


Fig. 7. A sample calibration curve for an Ultran NCT4-D13 Air-coupled piezoelectric receiver with a center frequency of 3.9 MHz (nominal 4 MHz). This plot demonstrates that at the transducer center frequency, a lower received force is necessary to generate a voltage than outside of the transducer bandwidth (lower value of F/V means more sensitive to impinging forces).

minum sample reflective for use with the Polytec LDV, the surface is polished to a mirror-like finish. The fused silica sample is partially covered with an extremely thin piece of aluminum reflective tape to achieve the same effect. The tape is thin enough that it does not contribute its own dynamics to the measurement, but provides an optically reflective surface for measurement.

The experimental data is recorded with a Tektronix TDS 5034B digital oscilloscope and recorded with a LabView script. The collected digital data is then later analyzed in MATLAB to extract the relative signal amplitudes.

3.2. Experimental procedure

The transducer was first applied to the bottom surface of the sample and clamped into place with a toggle clamp in order to ensure that the same clamping force and positioning is applied for each run of the experiment. A light oil was used as a couplant between the transducer and the sample to reduce contact nonlinearities and acoustic reflections.

The next step was to align the air-coupled transducer with respect to the sample surface. A standoff height of 5 mm was chosen between the face of the receiver and the sample as a compromise between signal strength and physical clearance issues through the entire experimental run. After setting the standoff height, the air-coupled transducer was aligned to the surface normal. The geometric alignment of the air-coupled transducer is by far the most challenging aspect of this measurement and also one of the most critical aspects. A small misalignment will cause noticeable defects in line and surface scans with the air-coupled transducer. For laser interferometry measurements, the process is simpler because the alignment is more forgiving. For a piston-like generating transducer, the scans should be symmetric, and this is one of the best criteria to use when evaluating adjustment impacts and determining future adjustments.

Once the air-coupled transducer is aligned normal to the surface, the total scan in the xy -plane is performed (typically a 20 mm by 20 mm scan with 0.5 mm measurement increments). Each measurement location is time averaged on the oscilloscope over 512 cycles to improve SNR. After the data is acquired, it is then processed in MATLAB.

3.3. Data processing

The MATLAB FFT algorithm is used to obtain the fundamental and second harmonic frequency components of the signal. In

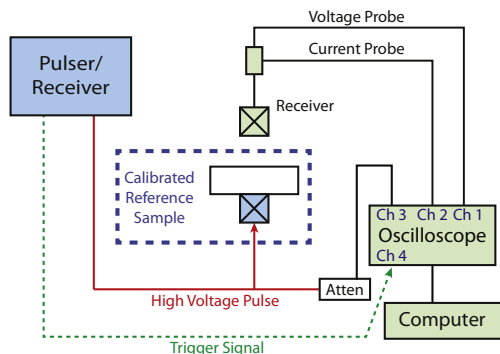


Fig. 6. A Schematic showing the calibration setup used in this work. Instead of a self-reciprocity calibration which is ineffective for air-coupled transducer at these frequencies, a calibrated reference sample is used along with the previously discussed MGB modeling framework to relate the predicted force on the receiver to the received voltage as a function of frequency.

measurements of relative signal amplitudes used to calculate measured of β^* , a Hann window is applied in the time domain to reduce the effects of amplifier and transducer transients. However, when the goal is to obtain amplitude-accurate signal components for the purpose of absolute nonlinearity measurements, the difficulty in correcting for amplitude and phase distortion of the signal is cumbersome. Numerous approaches to signal processing have been suggested, notably the use of IIR bandpass filters and convolution to obtain signal components with great success [45], but in this work it was determined that a simpler solution was to take the FFT of the steady state portion of the signal, treating it as if it were infinitely repeating and continuous. While seemingly trivial, the importance of choosing a suitable signal processing technique that accurately represents signal amplitude and phases cannot be overstated for absolute nonlinearity measurements. Once the signal amplitudes have been extracted at the frequencies of interest, the transducer calibration is applied to convert the values from electrical voltage to mechanical force.

The nonlinear least-squares curve fitting algorithm is then used to extract the modeling parameters according to Eq. (12). The steps in this process are similar to those used in earlier work [20]. The fundamental signal component is fit first using the framework outlined in Section 2.2 and Eq. (7) in order to extract the values of p_0 and α_1 . These values are then used as inputs to Eq. (8) in the fitting process for the second harmonic data, from which β is extracted.

4. Results and discussion

Air-coupled transducer and laser interferometer scanning measurement results are shown for the aluminum and fused silica samples in Fig. 8. Fig. 8(a) and (e) shows the fundamental and second harmonic scan results respectively measured by the air-coupled transducer from the aluminum specimen, while (b) and (f) show the laser interferometer surface scans from the same sample. The fundamental and second harmonic measurements in fused silica by the air-coupled transducer are shown in (c) and (g) respectively, with the corresponding laser interferometer measurements shown in (d) and (h). A few key features of the measurement are highlighted nicely in these images. First is the impact of alignment of the air-coupled transducer to the sample surface. In (a) and (e), the scan results are approximately radially symmetric, which is predicted by the modeling equations and shown to be empirically true on the sample surface by the laser interferometer scans in (b) and (f). This radial symmetry of the air-coupled transducer scan result indicates that the tilt of the transducer relative to the sample surface is well calibrated in both scan directions. In the fused silica scans shown in (c) and particularly in (g), the measurement result is slightly asymmetric. It is likely that the sample and the air-coupled transducer are misaligned along one or both axes, which is indicated by the comparison to the laser scans of (d) and (h) which show that the waveform at the surface of the sample is indeed radially symmetric. However, the use of the full-field measurement in the optimization process helps to reduce the impact of small misalignments such as those in Fig. 8(g).

Another observable effect from Fig. 8 is that the second harmonic measurement is much more directional and has a narrower main lobe than the fundamental measurement. This is a predictable result [44], but has experimental implications. Any misalignments are going to impact the second harmonic measurement more than the fundamental measurement for this reason. When performing the receiver alignment, generally there are two conditions that one must satisfy simultaneously. The first is that scans through the measurement center along the x and y axes are symmetric about the middle, and second is that the x and y scans are maximized at the same point (which becomes the

measurement center). If both of these conditions are met, then the result will be a clean scan and increased accuracy of the data processing and extraction of β .

After processing the data according to the algorithm outlined in Section 2.2, the resulting curves and matching laser interferometry measurements are shown in Fig. 9. Fig. 9(a) and (b) shows the results for the fundamental and second harmonic signals respectively from the aluminum specimen and (c) and (d) show the fundamental and second harmonic signal respectively from the fused silica specimen. Laser interferometry measurements are notoriously difficult for use in obtaining second harmonic amplitudes [34], one reason being the large error in measurements where the surface is imperfect in some way. This is clearly visible in Fig. 9(c) and (d) around 5 mm on the x axis of the plot from the large experimental error relative to the other measurement locations. While this is an important consideration, the relatively low error in the rest of the data points demonstrates sufficient surface quality for second harmonic measurements.

The fundamental aluminum results in Fig. 9(a) show very strong agreement with the interferometric measurements, as do the fundamental fused silica results in (c). The second harmonic aluminum results show strong agreement in the center of the measurement, but the side lobe information begins to deviate from the curve-fitting output. One reason for this could be the presence of generating transducer nonlinearity introduced from the Panametrics commercial source. The transmitter in the modeling proposed in this work is assumed to be a linear, piston-like source, such that a monochromatic input will lead to a monochromatic output. In reality, the generating transducer may also operate in a weakly nonlinear fashion, creating an additional propagating acoustic wave through the sample at the second harmonic frequency that propagates as a fundamental as in Eq. (7), referred to as the source nonlinearity [20]. This nonlinearity from the transducer can affect the measured second harmonic signal both in amplitude and in spatial distribution because the diffraction pattern of a fundamentally propagating wave displays a wider main lobe and more pronounced side lobe characteristics. This would explain the presence of the side lobe information in Fig. 9(b). Commercial transducers such as the one used in measuring the aluminum sample tend to have a higher source nonlinearity than single crystal piezoelectric disc sources, such as the LiNbO₃ disc used with the fused silica sample [2]. This assertion is strongly supported by the strong agreement of experimental results from the more linear source shown in Fig. 9(d) which does not display the variance between the measured side lobe information from the laser and air-coupled transducer.

Furthermore, a material with a higher nonlinearity such as fused silica, the generated material nonlinearity would more significantly overshadow the transducer nonlinearity. This would further justify the second harmonic results from the fused silica sample in Fig. 9(d) showing stronger agreement with the measured values than the aluminum sample in Fig. 9(b) given the presence of the transducer nonlinearity.

In the fused silica second harmonic results, the modeling shows strong correlation with measured values around the main lobe, and is more accurate regarding the side lobe predictions than in the aluminum sample as discussed previously. In particular, the geometric features of the curve-fit result match the features of the measured data, specifically the shapes and locations of the side lobes. The locations of these side lobes are related to the apparent radius of the generating transducer in the model, and hand-tuning this quantity can have the effect of matching these geometric features even more closely.

In order to calculate the acoustic nonlinearity parameter, the optimization algorithm discussed in Section 2.2 requires the calcu-

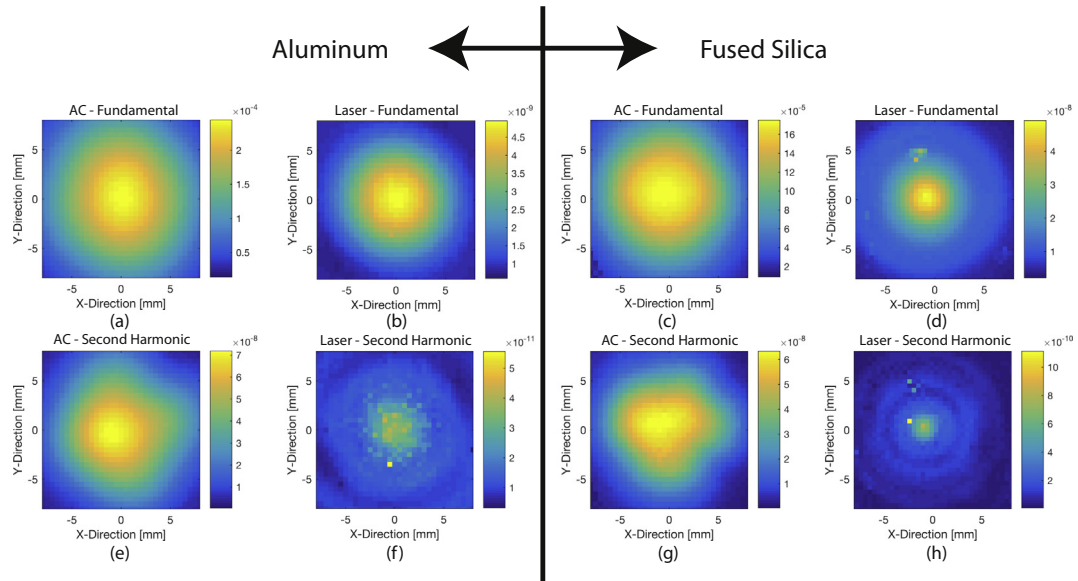


Fig. 8. Air-coupled transducer and laser interferometer scan results of aluminum and fused silica specimens. The aluminum fundamental (a) and second harmonic results (e) show strong radial symmetry characteristic of an accurate alignment of the air-coupled receiver. This is highlighted by the similarity to the laser interferometer scan results shown in (b) and (f). The air-coupled measurements in fused silica at the fundamental (c) and second harmonic (g) frequencies show more asymmetry in the second harmonic measurement as contrasted to the laser interferometer measurements in (d) and (h), indicating that improvements can be made to the air-coupled receiver alignment. These air-coupled measurements demonstrate what the air-coupled receiver “sees” when it area-weights the pressure field in air at each scan location.

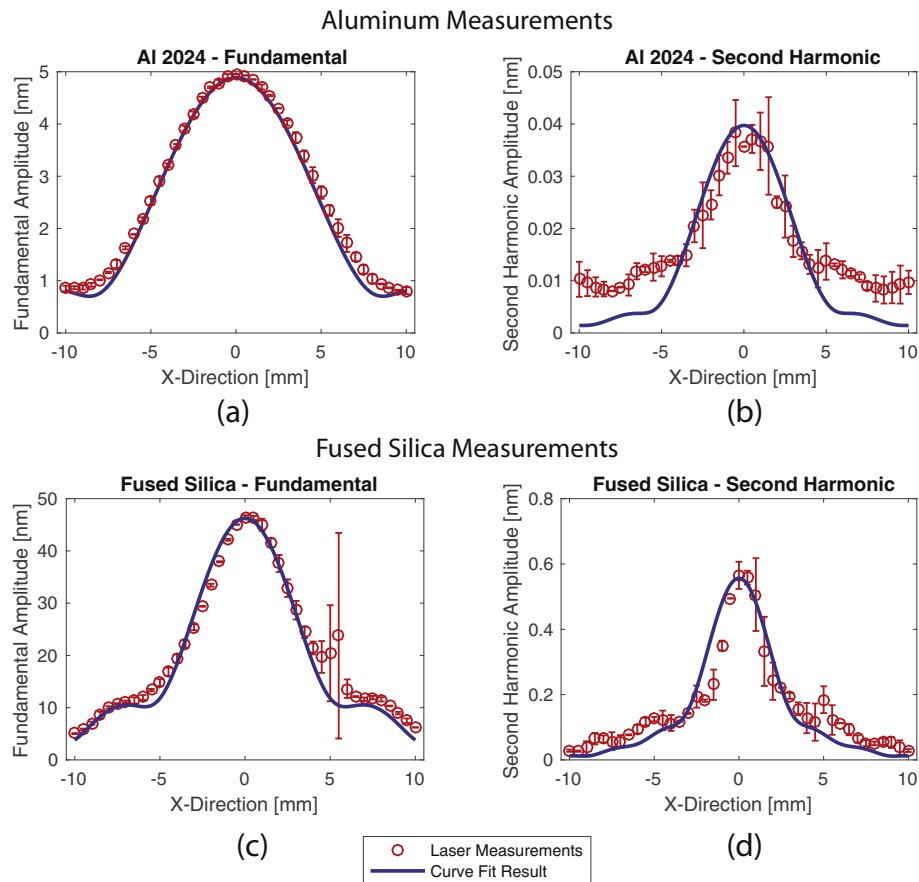


Fig. 9. Results of the nonlinear curve-fitting operation in aluminum and fused silica. The aluminum fundamental results (a) show very close alignment between the measured (red circle with error bars) and curve-fit (blue solid line) results, while the second harmonic (b) demonstrates very accurate results in the main lobe but differences in the side lobe amplitudes. The fused silica fundamental (c) is similarly accurate, while the second harmonic results (d) look much more like the modeling picture. The high variation in the fused silica data around the 5 mm measurement point is due to surface defects in the reflective tape used to make the laser interferometer measurement. (For interpretation of the references to color in this figure legend, the reader is referred to the web version of this article.)

lation of the other fitting parameters along with β . These parameters (p_0, α_1, α_2) are listed in Table 1.

An important observation that can be made from the modeling parameters obtained from the optimization algorithm is that the attenuation coefficients are extremely small in both aluminum and air. This results in nearly negligible attenuation corrections in the modeling. This conclusion aligns with expectations for frequencies below 10 MHz, where very low magnitude attenuation coefficients in similar metallic and fused silica specimens have been reported [2,6].

The major outcome of the optimization procedure is the value of the acoustic nonlinearity parameter β obtained from the model-based fitting of the experimental data. The use of the LiNbO₃ disc for generation of the input wave clearly reduces the source nonlinearity as can be seen in Fig. 9(d), which instills confidence in the optimization to calculate an accurate measure of β . The reported results in fused silica range from 9.7 to 14 [24,30,34,46], thus the measured β in this work of $12.1 \pm .5$ is in excellent agreement with literature values. Fused silica is very well studied in longitudinal NLU measurements, so agreement with literature values is a strong verification that the methods presented in this work provide accurate β estimates.

Values of β in aluminum from literature span a variety of heat treatments and thus have a large range of reported values from 4 to 12 [24,47,48]. That being said, the measured value of β in this work of 5.0 ± 0.3 , while falling in this range, is not a fully reliable estimate of the acoustic nonlinearity in the aluminum sample. The impact of source nonlinearity from the commercial transducer discussed earlier must be modeled more extensively or removed entirely through the use of an alternate source. Doing this will ensure that the measured second harmonic waveform is due primarily to second harmonic generation in the material and not from the measurement hardware. Electrical effects have thus far prevented the use of an LiNbO₃ disc (as in fused silica) with metallic samples to remedy this issue.

One final important consideration when using this approach is that the value of the nonlinearity parameter in some materials is known to be negative, producing a second harmonic out of phase with the fundamental wave form such as in fused silica [49]. This method obtains the magnitude of the nonlinearity parameter but does not obtain the phase relationship, and thus the result is the absolute value of the acoustic nonlinearity parameter for the material under test.

5. Conclusions and future work

In this work we have outline a modeling framework that allows for accurate calculation of the pressure field from the fundamental and second harmonic wave fields resulting from propagation through both a sample under test and the air column between the sample and the air-coupled receiver. These models account for attenuation and diffraction of the waves as they propagate through the combined stack of materials, and accounts for the various field components as they propagate across interfaces between these materials. By generating a new set of coefficients at each material interface, it is possible to extend this framework through any number of materials over any distance as long as there are suf-

ficient computational resources to complete the calculations. The use of MGB modeling makes this much more efficient than the use of a direct solution such as an RSI model, Which is very important for the extraction of β from measured data because of the iterative nature of the process.

In addition to proposing a modeling framework for pressure field calculation, a method for calibration air-coupled transducers is employed that circumvents the issues found with using self-reciprocity calibration methods as is standard for use with contact piezoelectric transducers. This calibration method employs the use of a calibration sample and the modeling framework proposed in this work, and was shown to produce results that are in agreement with those expected of resonant piezoelectric, narrow-band devices. A sample calibration curve confirms the resonance of the 4 MHz transducers to be closer to 3.9 MHz, which aligns with its observed behavior.

The modeling framework proposed in this work was used in a nonlinear optimization algorithm employing a least-squares curve-fitting technique which allows for the extraction of the absolute nonlinearity parameter β when combined with the air-coupled transducer calibration. This method was demonstrated by measuring β for two materials: aluminum 2024 and fused silica. The measured β value in the aluminum sample agrees with literature values but includes significant contributions from other sources of nonlinearity, and the measured β value in fused silica agrees with literature values in a strongly convincing fashion because of the low source nonlinearity of the lithium niobate transmitter. The agreement with the extracted values of β from the methods proposed in this work with those found in literature, particularly in the case of the fused silica result, validates the use of this framework for using air-coupled transducers to determine the absolute nonlinearity parameter in a non-contact environment.

There are many aspects of this measurement that can be improved, such as the automation of the alignment of the air-coupled transducer to the sample surface. As of now, the hand-tuning process is very labor intensive and fickle, and often the success of the alignment can take several hours to accomplish. By automating this process through the use of some optimization procedure such a conjugate gradients approach to rapidly converge on the proper air-coupled transducer orientation, this can be made into a relatively simple procedure. Doing this would require the mechanization of the rotation stages and height adjustment for CNC control, which is beyond the capability and funds of the current work.

Additionally, the disagreement between aspects of the modeled wave fields and measure wave fields can be attributed to a variety of possible reasons which are worth exploring in further detail. It was proposed in previous work [20] that the generating transducer can, for whatever reason, introduce a generated transducer nonlinearity which acts as a fundamentally propagating wave (e.g. monotonically decreasing) at the second harmonic frequency of 2ω . The presence of this wave field component would explain the increased side lobe presence in aluminum line scan results, as those side lobes match the results of a linearly propagating field components. The relative strengths of the transducer generated nonlinearity to the material generated nonlinearity could be estimated by careful calibration of the generating transducer, and could also be added to the curve-fitting operation by using a cost function that takes this generating transducer nonlinearity into account. This would provide the complete modeling picture, but would likely require careful tuning of the optimization process to deal with the added cost function complexity.

Finally, this technique would be even more valuable to the NDE community if it could be applied to Rayleigh wave measurements, which would allow for absolute β measurement from one-sided material access, greatly increasing the viability of this technique

Table 1
Optimization variables for aluminum and fused silica specimens as a result of the process outlined in Section 2.2

Material	p_0 (Pa)	$\alpha_1 \left(\frac{Np}{m} \right)$	$\alpha_2 \left(\frac{Np}{m} \right)$
Al 2024	9.57e5	2.3e−3	8.1e−3
Fused Silica	4.12e5	6.9e−3	1.4e−2

in hazardous or otherwise difficult environments. This would require adapting the modeling of the wave-fields to Rayleigh wave propagation and harmonic generation, but otherwise the framework proposed in this work would remain largely unchanged. This would make air-coupled transducers a fully viable technology for NLU measurements in field applications, and would be a valuable addition to the NDE toolbox.

Acknowledgments

We would like to acknowledge the NSF [Grant No. 1362204] for funding this work.

References

- [1] J. Herrmann, J.-Y. Kim, L.J. Jacobs, J. Qu, J.W. Little, M.F. Savage, Assessment of material damage in a nickel-base superalloy using nonlinear Rayleigh surface waves, *J. Appl. Phys.* 99 (12) (2006), pp. 124913–124913.
- [2] J.-Y. Kim, L.J. Jacobs, J. Qu, J.W. Little, Experimental characterization of fatigue damage in a nickel-base superalloy using nonlinear ultrasonic waves, *J. Acoust. Soc. Am.* 120 (3) (2006) 1266–1273.
- [3] S.V. Walker, J.-Y. Kim, J. Qu, L.J. Jacobs, Fatigue damage evaluation in a36 steel using nonlinear Rayleigh surface waves, *NDT & E Int.* 48 (2012) 10–15.
- [4] T. Apple, J. Cantrell, C. Amaro, C. Mayer, W. Yost, S. Agnew, J. Howe, Acoustic harmonic generation from fatigue-generated dislocation substructures in copper single crystals, *Phil. Mag.* 93 (21) (2013) 2802–2825.
- [5] M. Liu, J.-Y. Kim, L. Jacobs, J. Qu, Experimental study of nonlinear Rayleigh wave propagation in shot-peened aluminum plates—feasibility of measuring residual stress, *NDT & E Int.* 44 (1) (2011) 67–74.
- [6] A. Ruiz, N. Ortiz, A. Medina, J.-Y. Kim, L. Jacobs, Application of ultrasonic methods for early detection of thermal damage in 2205 duplex stainless steel, *NDT & E Int.* 54 (2013) 19–26.
- [7] D. Barnard, G. Dace, O. Buck, Acoustic harmonic generation due to thermal embrittlement of inconel 718, *J. Nondestr. Eval.* 16 (2) (1997) 67–75.
- [8] J.S. Valluri, K. Balasubramaniam, R.V. Prakash, Creep damage characterization using non-linear ultrasonic techniques, *Acta Mater.* 58 (6) (2010) 2079–2090.
- [9] K. Matlack, J. Wall, J.-Y. Kim, J. Qu, L. Jacobs, H.-W. Viehrieg, Evaluation of radiation damage using nonlinear ultrasound, *J. Appl. Phys.* 111 (5) (2012), pp. 054911–054911.
- [10] M. Breazeale, D. Thompson, Finite-amplitude ultrasonic waves in aluminum, *Appl. Phys. Lett.* 3 (5) (1963) 77–78.
- [11] A. Gedroitz, V. Krasilnikov, L. Zarembo, Elastic waves of finite amplitude in solids and anharmonicity of the lattice, *Acta Acust. United Acust.* 13 (2) (1963) 108–110.
- [12] M. Breazeale, J. Ford, Ultrasonic studies of nonlinear behavior of solids, *J. Appl. Phys.* 36 (11) (1965) 3486, <http://dx.doi.org/10.1063/1.1703023>.
- [13] A. Hikata, B.B. Chick, C. Elbaum, Dislocation contribution to the second harmonic generation of ultrasonic waves, *J. Appl. Phys.* 36 (1) (1965) 229–236.
- [14] A. Hikata, C. Elbaum, Generation of ultrasonic second and third harmonics due to dislocations. i, *Phys. Rev.* 144 (2) (1966) 469.
- [15] D. Thompson, O. Buck, R. Barnes, H. Huntington, Diffusional properties of the stage-iii defect in copper. i. Experimental results, *J. Appl. Phys.* 38 (8) (1967) 3051–3056.
- [16] D. Thompson, O. Buck, H. Huntington, P. Barnes, Diffusional properties of the stage-iii defect in copper. ii. A model for defect-dislocation interactions, *J. Appl. Phys.* 38 (8) (1967) 3057–3067.
- [17] W.B. Gauster, M. Breazeale, Ultrasonic measurement of the nonlinearity parameters of copper single crystals, *Phys. Rev.* 168 (3) (1968) 655.
- [18] A. Viswanath, B.P.C. Rao, S. Mahadevan, P. Parameswaran, T. Jayakumar, B. Raj, Nondestructive assessment of tensile properties of cold worked AISI type 304 stainless steel using nonlinear ultrasonic technique, *J. Mater. Process. Technol.* 211 (3) (2011) 538–544.
- [19] S. Thiele, J.-Y. Kim, J. Qu, L.J. Jacobs, Air-coupled detection of nonlinear Rayleigh surface waves to assess material nonlinearity, *Ultrasonics* 54 (6) (2014) 1470–1475.
- [20] D. Torello, S. Thiele, K.H. Matlack, J.-Y. Kim, J. Qu, L.J. Jacobs, Diffraction, attenuation, and source corrections for nonlinear Rayleigh wave ultrasonic measurements, *Ultrasonics* 56 (2015) 417–426.
- [21] D.C. Hurley, D. Balzar, P.T. Purtscher, Nonlinear ultrasonic assessment of precipitation hardening in ASTM a710 steel, *J. Mater. Res.* (2000) 2036–2042.
- [22] C. Desilets, J. Fraser, G.S. Kino, The design of efficient broad-band piezoelectric transducers, *IEEE Trans. Son. Ultrason.* 25 (3) (1978) 115–125.
- [23] G.S. Kino, *Acoustic Waves: Devices, Imaging, and Analog Signal Processing*, vol. 107, Prentice-Hall, Englewood Cliffs, NJ, 1987.
- [24] G.E. Dace, R.B. Thompson, O. Buck, Measurement of the acoustic harmonic generation for materials characterization using contact transducers, in: *Review of Progress in Quantitative Nondestructive Evaluation*, vol. 11B, vol. 11, 1992, pp. 2069–2076.
- [25] G. Dace, R.B. Thompson, L.J. Brasche, D.K. Rehbein, O. Buck, Nonlinear acoustics, a technique to determine microstructural changes in materials, in: *Review of Progress in Quantitative Nondestructive Evaluation*, Springer, 1991, pp. 1685–1692.
- [26] A.L. Lopez-Sanchez, L.W. Schmerr Jr., Determination of an ultrasonic transducer's sensitivity and impedance in a pulse-echo setup, *IEEE Trans. Ultrason. Ferroelectrics Freq. Control* 53 (11) (2006) 2101–2112.
- [27] L. Sun, S.S. Kulkarni, J.D. Achenbach, S. Krishnaswamy, Technique to minimize couplant-effect in acoustic nonlinearity measurements, *J. Acoust. Soc. Am.* 120 (5) (2006) 2500–2505.
- [28] M. Treiber, J.-Y. Kim, L.J. Jacobs, J. Qu, Correction for partial reflection in ultrasonic attenuation measurements using contact transducers, *J. Acoust. Soc. Am.* 125 (2009) 2946.
- [29] J. Cantrell, K. Salama, Acoustoelastic characterisation of materials, *Int. Mater. Rev.* 36 (1) (1991) 125–145.
- [30] D. Hurley, C. Fortunko, Determination of the nonlinear ultrasonic parameter using a Michelson interferometer, *Meas. Sci. Technol.* 8 (6) (1997) 634.
- [31] W.T. Yost, J.H. Cantrell, Anomalous nonlinearity parameters of solids at low acoustic drive amplitudes, *Appl. Phys. Lett.* 94 (2) (2009) 1905.
- [32] H. Ogi, M. Hirao, S. Aoki, Noncontact monitoring of surface-wave nonlinearity for predicting the remaining life of fatigued steels, *J. Appl. Phys.* 90 (1) (2001) 438–442.
- [33] A. Cobb, M. Capps, C. Duffer, J. Feiger, K. Robinson, B. Hollingshaus, Nonlinear ultrasonic measurements with EMATs for detecting pre-cracking fatigue damage, *Review of Progress in Quantitative Nondestructive Evaluation: Volume 31*, vol. 1430, AIP Publishing, 2012, pp. 299–306.
- [34] A. Moreau, Detection of acoustic second harmonics in solids using a heterodyne laser interferometer, *J. Acoust. Soc. Am.* 98 (5) (1995) 2745–2752.
- [35] A. Ruiz, P.B. Nagy, Laser-ultrasonic surface wave dispersion measurements on surface-treated metals, *Ultrasonics* 42 (1–9) (2004) 665–669.
- [36] C.B. Scruby, L.E. Drain, *Laser Ultrasonics Techniques and Applications*, CRC Press, 1990.
- [37] K. Matlack, J.-Y. Kim, L. Jacobs, J. Qu, Review of second harmonic generation measurement techniques for material state determination in metals, *J. Nondestr. Eval.* (2014) 1–23.
- [38] E. Zabolotskaya, R. Khokhlov, Quasi-plane waves in the nonlinear acoustics of confined beams, *Sov. Phys. Acoust.* 15 (1) (1969) 35–40.
- [39] D. Huang, M. Breazeale, A gaussian finite-element method for description of sound diffraction, *J. Acoust. Soc. Am.* 106 (4) (1999) 1771–1781.
- [40] J. Wen, M. Breazeale, A diffraction beam field expressed as the superposition of gaussian beams, *J. Acoust. Soc. Am.* 83 (5) (1988) 1752–1756.
- [41] R. Huang, Ultrasonic modeling for complex geometries and materials (Ph.D. thesis), Iowa State University, 2006.
- [42] S. Zhang, H. Jeong, S. Cho, X. Li, Simultaneous evaluation of acoustic nonlinearity parameter and attenuation coefficients using the finite amplitude method, *AIP Adv.* 5 (7) (2015) 077133.
- [43] H. Jeong, S. Zhang, D. Barnard, X. Li, Significance of accurate diffraction corrections for the second harmonic wave in determining the acoustic nonlinearity parameter, *AIP Adv.* 5 (9) (2015) 097179.
- [44] L.E. Kinsler, A.R. Frey, A.B. Coppens, J.V. Sanders, *Fundamentals of Acoustics*, fourth ed., John Wiley & Sons, Hoboken, NJ, 1999.
- [45] D.J. Barnard, S.K. Chakrapani, Measurement of nonlinearity parameter (β) of water using commercial immersion transducers, 42nd Annual Review of Progress in Quantitative Nondestructive Evaluation: Incorporating the 6th European-American Workshop on Reliability of NDE, vol. 1706, AIP Publishing, 2016, p. 060004.
- [46] J.H. Cantrell Jr, M. Breazeale, Ultrasonic investigation of the nonlinearity of fused silica for different hydroxyl-ion contents and homogeneities between 300 and 3 °K, *Phys. Rev. B* 17 (12) (1978) 4864.
- [47] P. Li, W. Yost, J. Cantrell, K. Salama, Dependence of acoustic nonlinearity parameter on second phase precipitates of aluminum alloys, in: *IEEE 1985 Ultrasonics Symposium*, 1985, pp. 1113–1115.
- [48] W.T. Yost, J.H. Cantrell, The effects of artificial aging of aluminum 2024 on its nonlinearity parameter, in: D.O. Thompson, D.E. Chimenti (Eds.), *Review of Progress in Quantitative Nondestructive Evaluation*, Springer, 1993, pp. 2067–2073.
- [49] J.A. Bains Jr., M. Breazeale, Nonlinear distortion of ultrasonic waves in solids: approach of a stable backward sawtooth, *J. Acoust. Soc. Am.* 57 (3) (1975) 745–746.